International Journal of Science and Research (IJSR)
ISSN: 2319-7064
SJIF (2022): 7.942

Electrochemical Properties of Fe Doped $NiCo_2O_4$ Synthesised by Low-Temperature Microwave Hydrothermal Process

Satyanarayana Maheshwaram[1], Rakesh Kumar Thida[2], Shilpa Chakra Chidurala[3], Venkata Narayana M[4], Ravinder Reddy Butreddy[5]

[1, 4, 5]Department of Physics, University College of Science, Osmania University, Hyderabad, Telangana, India

[2, 3]Centre for Nano Science and Technology, Jawaharlal Nehru Technological University, Hyderabad, Telangana, India

[5]Corresponding author Email: *ravinderbutreddy[at]gmail.com*

Abstract: ***In this study, $NiFe_xCo_{2-x}O_4$ (FNCO) nanoparticle samples were prepared using the microwave hydrothermal technique, for x = 0.0, 0.02, 0.04, 0.06, 0.08, and 0.10, XRD, SEM, EDX, XPS, and FTIR were used to characterize the samples. The XRD shows all samples formed the cubic-spinel structure with the spatial group Fd-3m. The dip coating technique was used to fabricate the anode electrodes of $NiFe_xCo_{2-x}O_4$ samples. Cyclic voltammetry was used to investigate the electrochemical characteristics of CV, GCD, and EIS. The Specific capacitance of x = 0.06 composition, showed superior GCD characteristics with a highest specific capacitance of 640.06 F g^{-1} at a current density of 1 A g^{-1} and it was found that with the increase in frequency, the conductivity was increased.***

Keywords: Electrochemical, Spinel, Microwave hydrothermal, dip coating, carbon mesh

1. Introduction

It is imperative that researchers investigate renewable resources to address the ever-rising energy usage [1-3]. These days, it appears that the growth of renewable resources is causing a rise in the demand for electrochemical energy storage [4]. To meet the development, a number of energy storage techniques have been suggested [5]. Due to their fast kinetic, high-power density, extremely long lifetime, and high coulombic efficiency, supercapacitors (SCs) are thought to be a type of energy storage apparatus with significant potential [6]. In addition, SCs have a great deal of promise to replace lithium batteries and be used in a variety of applications, including pacemakers, hybrid electric vehicles, and so forth [7]. It is common knowledge that the electrode materials have a major impact on the characteristics of SCs. Different materials have been widely studied as SC electrode materials until this point, including carbonaceous materials, transition metal oxides [8], conductive polymers [9], and hybrid composites [10]. Researchers from all over the world are trying to increase the ability of electrical batteries to store energy. Researchers have extensively investigated composites of $NiCo_2O_4$ to increase the energy storage capacity of Li-Ion batteries. The research of various electrode materials has received a lot of attention [11]. Numerous uses, including sensing, catalysis, energy conversion, and storage, were drawn to the distinctive morphologies of carbons and their thermal, mechanical, and chemical stability [12]. In addition, recently, spinel nickel cobaltite ($NiCo_2O_4$) has been suggested to be a potential electrode material owing to the charming preponderances, such as the high specific capacitance, low-price as well as affluent reserves. Particularly, electric conductivity and electrochemical activity of $NiCo_2O_4$ are superior to those of either NiO or Co_2O_3 [13]. Thus, it can apply in diverse fields, for instance supercapacitors [14], lithium-ion batteries [15], photodetectors [16], electrocatalysis [17], ferrofluid technology [18], etc. So far, various methods (sol-gel [19], electro-deposition [20], microwave [21], hydrothermal synthesis [22], etc. have been adopted to synthesize the $NiCo_2O_4$ with different morphologies, including nanowires, nanoneedles [23], nanoparticles [24] and nanosheet [25]. However, there is a tremendous challenge to synthesize a complex structure assembled by nano-scaled building blocks [26].

A significant amount of research has already been conducted on the impact of Fe substitution in NCO NPs on gas sensing properties, as an electrocatalyst is, electrodes in batteries and supercapacitors [27-28]. As a result, because of its high theoretical capacity, non-flammable native, and cheap cost, spinel-type Nickel cobalt oxide ($NiCo_2O_4$) has attracted attention [29]. However, some issues continue to impede the commercialization of $NiCo_2O_4$ as the anode material in lithium-ion batteries for electric cars (EVs). The structural collapse of the $NiCo_2O_4$ during the intercalation and extraction of the lithium ion will cause the capacity fade and poor cycling stability [30]. This will be the first effect of the severe volume change of the material. Second, the poor electric conductivity of $NiCo_2O_4$ can reduce the ion diffusion rate at high current densities, preventing EVs from meeting their high-power density requirement. Designing transition metal oxide composites for improving lithium storage performance, on the other hand, is a viable approach [31]. Due to their low activation energy for electron transfer between cations, composites of bimetal oxide and partially doped metal oxides have been shown to have much better electrochemical performance than single ones [32-34]. $NiA_xCo_{2-x}O_4$ (A = Cu, Zn, Fe, Mn) anode materials have been extensively used in recent years. However, according to the published literature, the impact of Co substitutions on microwave absorption and electrochemical properties and structural properties with Fe has received little attention.

2. Experimental

All the reagents (Sigma-Aldrich Chemicals, Bangalore, India) were analytically pure without further treatment. The different synthesis methods were reported for the preparation of Nickel cobalt oxides [35-38], even though each method has its own advantages and disadvantages.

The microwave hydrothermal (MH) technique was used to prepare the nickel cobalt oxides with Fe doping in this study. In this technique, five samples of 10 mg each were prepared by adding Fe to Nickel cobalt oxides. Nickel nitrate ($NiNO_3$), Cobalt nitrate ($CoNO_3$), Iron chloride ($FeCl_3$. $4H_2O$), and sodium hydroxide (NaOH) were dissolved stoichiometrically in 30 cc of doubly purified water and thoroughly combined. For 30 minutes, the above fluid was constantly stirred until a uniform combination formed. After stirring, the solution was poured into CEM MARSXPRESS 230/60 containers for the microwave hydrothermal procedure. The MH process was maintained at 60 °C for 40 minutes,. The precipitate was produced during the procedure, and all samples were filtered and washed numerous times with deionized water and ethanol. After cleaning, the nanoparticles samples were dried overnight in an oven set to 80 degrees Celsius. The desiccated powders were then calcined in a muffle furnace at 600 °C for 4 hours. In this synthesis, the particles obtained are $NiFe_xCo_{2-x}O_4$ nanoparticles (FNCO NPs) for x = 0.0, 0.02, 0.04, 0.06, 0.08, and 0.10 of six samples.

The FNCO NPs were prepared to fabricate the working anode. In this study, we used 80% active material (FNCO NPs), 10% polyvinylidene fluoride (PVDF), 10% activated carbon, and wire mesh for electrode fabrication. PVDF is immune to unfavourable weather conditions over a broad temperature range, has excellent chemical resistance to electrodes, and is an organic binder. Activated carbon is used as a solvent to increase the biologically active surface area and restrict the adsorbent at the electrode-electrolyte contact. The combined active material (FNCO), PVDF, and Activated carbon material combination was produced as a viscous slurry using a mortar and pestle [39] with a few droplets ofN-Methyl-2-pyrrolidone (NMP) and coated on a 1.91 cm^2 Ni foam substrate (purity 99.9%, cm^2 Ni foam substrate (purity 99.9%, thickness2 mm, PPI (60–90) %, pore size 0.05– 0.5 mm) uniformly and heated to 80^{o}C for 12 hours.

The Crystal information of the samples was acquired by Bruker D8 Discover X-ray diffractometer (XRD) (SHIMADZU, XRD-7000, Tokyo, Japan) with Cu Kα radiation (λ = 1.5406 Å). Microstructures, particle sizes and element mapping were analysed by using a JEOL-7100F, Scanning electron microscope (SEM, Hitachi, Japan.TheFourier transform infrared spectroscopy (FTIR) (SHIMADZU, 8400S) was used tofind functional groups and determining bonding informationof the samples. The elemental and chemical states of the sample were analyzed by a Kratos Axis Ultra DLD X-ray photoelectron spectrometer (XPS, VG, Manchester, UK). The Cyclic voltammetry (CV), Galvanometer Charge and Discharge (GCD), Impedance studies also studied to know about electrochemical properties.

The electrochemical analysis was performed by a three-electrode system using a Metrohm Autolab PGSTA302N (Potentiostat/Galvanostat) equipment with NOVA 2.0.2 software was used to electrochemically characterize the samples in 2 M KOH. FNCO NPs, Ag/AgCl, and Pt foilwere used asthe working, reference, and counter electrodes respectively. Electrochemical impedance spectroscopy (EIS) tests were conducted in the 0.01–100 kHz frequency range, with potential amplitude of 5 mV. The CV test was carried out in a -0.1 – 0.4 V potential window at 5, 10, 15, 20 and 25 mVs^{-1}. Galvanostatic charge–discharge experiments were performed in a 0 – 1.0 V potential range at a current density of1 Ag^{-1}.

The specific capacitance (C_s)is calculated using CV studies by adopting the relation [38]:

$$C_s = \frac{I\Delta t}{m\Delta V} \qquad F\ g^{-1} \text{ ------- (1)}$$

where m, Δt, ΔV, and I are the mass of active material, total discharge time, voltage drop through the discharge process and the discharge current respectively.

3. Results and Discussions

The X-ray diffraction (XRD) phase study of FNCO for x = 0.0, 0.02, 0.04, 0.06, 0.08 and 0.10 compositions is shown in Fig. 1. XRD is used to validate the crystallite phase information of various FNCOsamples. The XRD spectra indicate that this microwave hydrothermal technique provides a nearly pure NCO [40]. The crystallite has a face-centred cubic spinel structure with the spatial group Fd-3m and the unit cell dimension of the spinel structure, lattice parameter(a), was calculated from the measured d-spacing for the planes:

$$a = d\sqrt{(h^2+k^2+l^2)} \quad Å \text{ ---------- (2)}$$

where h, k and l are the Miller indices.and calculated the parameters with the help of equation following equations:

The average Crystal size using Debye Scherrer's formula[41],

$$\langle D\rangle = 0.9\,\lambda/\beta\cos\theta \qquad nm \text{ --------- (3)}$$

and

The X-ray density,

$$\rho = ZM/Na^3 \qquad gcm^{-3} \text{ ------- (4)}$$

where k is a constant and is 0.9 for spherical particles, λ is the wavelength of X-rays (1.5406 Å), β is the full width at half maxima in radians, θ is the diffraction angle.

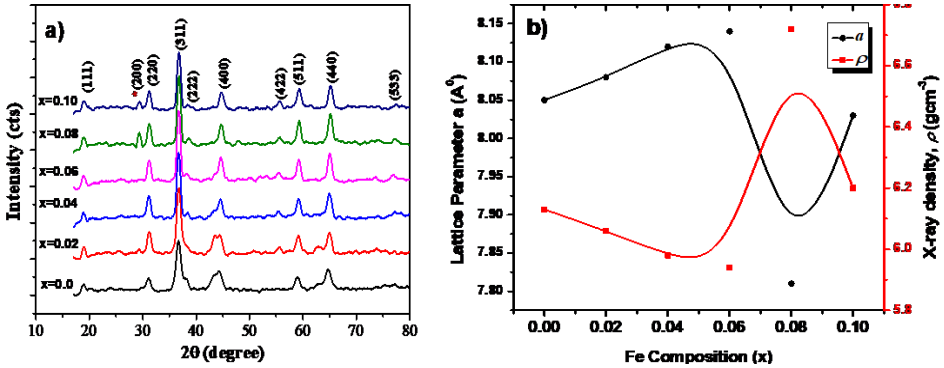

Figure 1: a). XRD pattern of FNCO NPs for x = 0.0, 0.02, 0.04, 0.06, 0.08 and 0.10, b). Graph showing Zn composition (x) versus Lattice parameter (a) and X-ray density (ρ).

The lattice parameters and the graph in Fig. 1(a) indicate that the sample is more crystal in nature. The h, k, l value (200) arises due to the dopant element Fe. The lattice parameter, (a) found to be high at Fe = 0.06 with the lattice parameter 8.14 Å and then increases slowly and then decreases sharply and again increases. This is due to the fact that the Co ions have lower molar mass (28.01 g/mol) being replaced with the greater molar mass (55.845 g/mol) Fe cation. Fig. 1(b) revealed that the variation of X-ray density has reverse variation tendency compared to the variation of lattice constant, considering that the X-ray density inverse to the lattice constant.

The calculated unit cell parameter values are shown in Table 1. These values are close to the 0.8 nm value mentioned in the ICSD collection codes for FNCO: 01-073-1704 and 00-001-1152. The Scherer equation was used to compute the average crystallite sizes of the composites, and the crystal size was steadily raised up to x= 0.04, then dropped size and increased again up to 54.56 nm.The Scherer equation was used to compute the average crystallite sizes of the composites. The resulting samples were crystalline, and the diffraction lines can be indexed to cubic spinel NCO.

The vibrational modes exhibited by different functional groups of FNCO were investigated by FTIR analysis and the corresponding graphs were shown in the Fig. 2. A broad peak observed at 3442 cm^{-1} is attributed to OH-stretching vibrations and the band observed at 1379 $cm^{-1}$and 1387 cm^{-1}. These are belonging to OH-bending vibrations.

Table 1: The calculated parameters of Lattice constant (a) and Average crystallite size (<D>), and X-ray density (ρ) of FNCO NPs for x = 0.0, 0.02, 0.04, 0.06, 0.08 and 0.10.

S. No.	Fe doping, x	Lattice Parameter $a = d\sqrt{(h^2+k^2+l^2)}$ Å	Crystal size <D> = 0.9 λ/β cos θ nm	X- ray density $\rho = ZM/Na^3$ (gcm^{-3})
1	0.00	8.05	27.27	6.13
2	0.02	8.08	36.53	6.06
3	0.04	8.12	36.33	5.98
4	0.06	8.14	27.24	5.94
5	0.08	7.81	36.49	6.72
6	0.10	8.03	54.56	6.20

The distinctive metal oxygen vibration peaks were detected at 663 and 559 cm^{-1}, respectively, and the impact of Fe doping in NCO results in a decrease in relative strength of peaks, which may be due to crystal structure disorder caused by dopant incorporation. However, with the addition of Fe-doping, the impact of the individual elements is neutralized, resulting in more oxygen vacancies in NCO NPs.

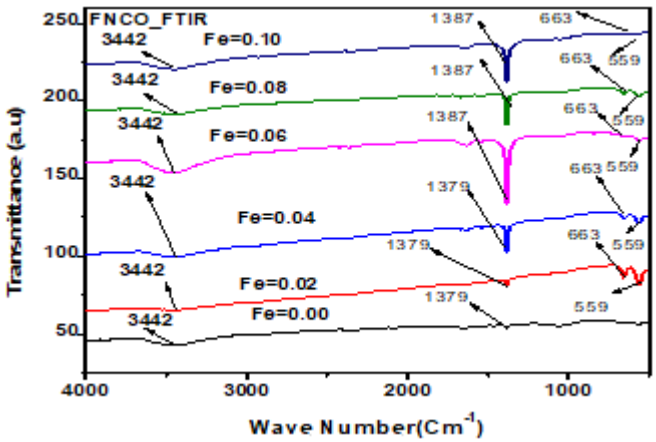

Figure 2: Fourier Transform Infrared spectra of FNCO NPs for x = 0.0, 0.02, 0.04, 0.06, 0.08 and 0.10

The scanning electron microscopy (SEM) and electron dispersive X-ray (EDX) spectra of FNCO for x = 0.0, 0.02, 0.06, and 0.10 compositions are shown in Fig. 3(a-d) and Fig. 4(a-d). All the figures indicate that the sample under

investigation have an average size of 112 nm. The EDAX analysis conformsthat all elements were presentand is without impurity.

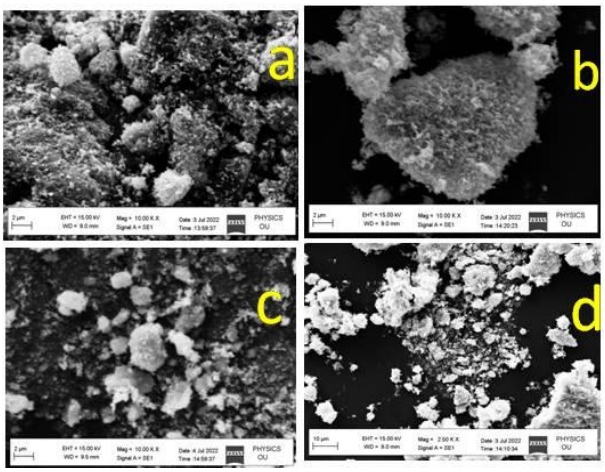

Figure 3 (a-d): SEM images of the elemental compositions of FNCO NPs for x = 0.0, 0.02, 0.06 and 0.10.

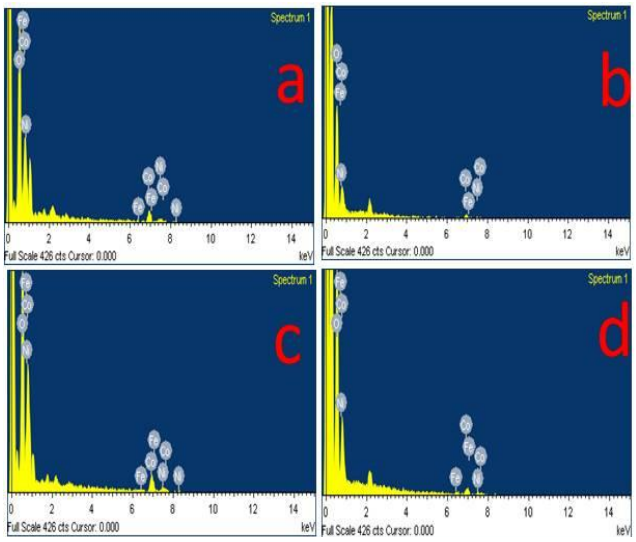

Figure 4 (a-d): EDAX images of the elemental compositions of FNCO NPs for x = 0.0, 0.02, 0.06 and 0.10

The XPS analysis was used to acquire more comprehensive information on the chemical composition and associated oxidation states of the individual catalyst surfaces. Fig. 5 and 6 shows the corresponding spectrums.

The Ni 2p spectrum is fitted using Gaussian fitting, considering two spin-orbit doublets characteristic of Ni^{2+} and Ni^{3+}, as well as two shakeup satellites. Fitting peaks with binding energies ranging from 861.64 eV to 871.97 eV are assigned to Ni $2p_{1/2}$, whereas fitting peaks at binding energies ranging from 854.46 eV to 854.81 eV are assigned to Ni $2p_{3/2}$. Two types of Co species are also seen in the Co 2p spectra. The fitting peaks at 890.13 eV to 795.3 eV are indexed to Co $2p_{1/2}$, whereas the other fitting peaks at 785.17 eV to 779.3 eV are indexed to Co $2p_{3/2}$. In addition, the Co^{3+}/Co^{2+} coexisted in the core-shell. Table 2 summarises the energy of the samples.

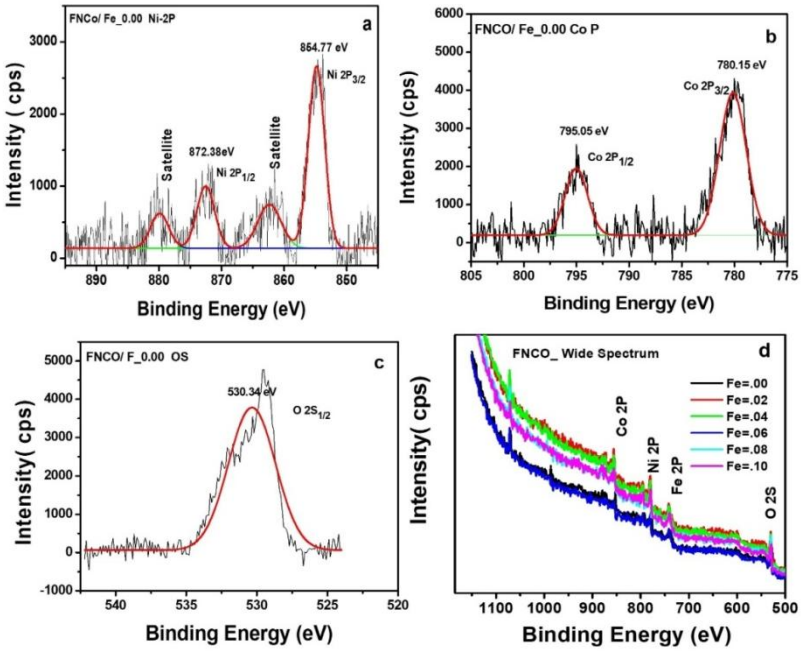

Figure 5 (a-d): X-ray Photoelectron Spectroscopy (XPS) of FNCO NPs showing the Binding energy vs Intensity of a). Ni, b) Co, c). O for x = 0.0 and d). Wide spectrum of FNCO deconvoluted graph.

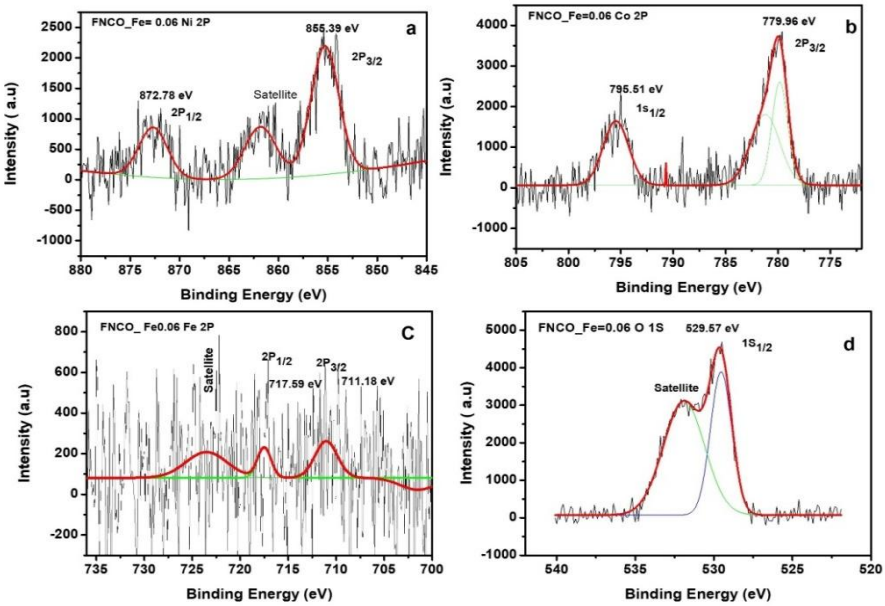

Figure 6 (a-d): X-ray Photoelectron Spectroscopy (XPS) of FNCO NPs showing the Binding energy vs Intensity of a). Ni, b). Fe, c). Co, and d). O deconvoluted graph for x = 0.06

Table 2: The values of band gap energies of the compositions Fe, Co, Ni and O of their orbital states of FNCO NPs for x = 0.0, 0.02, 0.04, 0.06, 0.08 and 0.10.

Sl. No.	Binding energy(eV)of FNCO NPs							
	Fe doping, x	Ni		Co		Fe		O
		$2p_{1/2}$	$2p_{3/2}$	$2p_{1/2}$	$2p_{3/2}$	$2p_{1/2}$	$2p_{3/2}$	$1s_{1/2}$
1	0.00	861.64	854.46	790.13	785.17	---	---	530.35
2	0.02	872.43	855.14	795.5	780.4	717.86	711.26	530.2
3	0.04	872.87	855.22	795.59	780.41	717.86	711.26	528.39
4	0.06	872.78	855.39	795.51	779.96	717.59	711.18	529.57
5	0.08	872.48	854.93	795.02	780.13	718.15	710.62	529.81
6	0.10	871.97	854.81	795.78	779.3	720.15	716.29	529.81

The electrochemical properties of the electro catalyst samples were determined using cyclic voltammetry (CV), galvanostatic charge/discharge (GCD), and electrochemical impedance spectroscopy (EIS) in a three-electrode configuration. CV is a best technique to analyse the electrochemical performance of any active component and were obtained at a potential ranging from -0.1 to 0.4 V.

To study the redox interaction between metallic ions and aqueous electrolytic solution, the CV analysis was conducted on the working electrodes at various scan rates (5-25 mVs^{-1}) in the potential range -0.1-0.4V, as shown in Fig. 7 (a-f).The shapes of the CV profile deviated from ideal rectangle; clearly signify the pseudo capacitive nature of FNCO NPs produced by electrochemical reactions at the electrode surface. It is noticed that the profile of the CV plot does not appear to alter significantly even at large scan rates and the total charge accumulation increases with increasing scan rates [42].

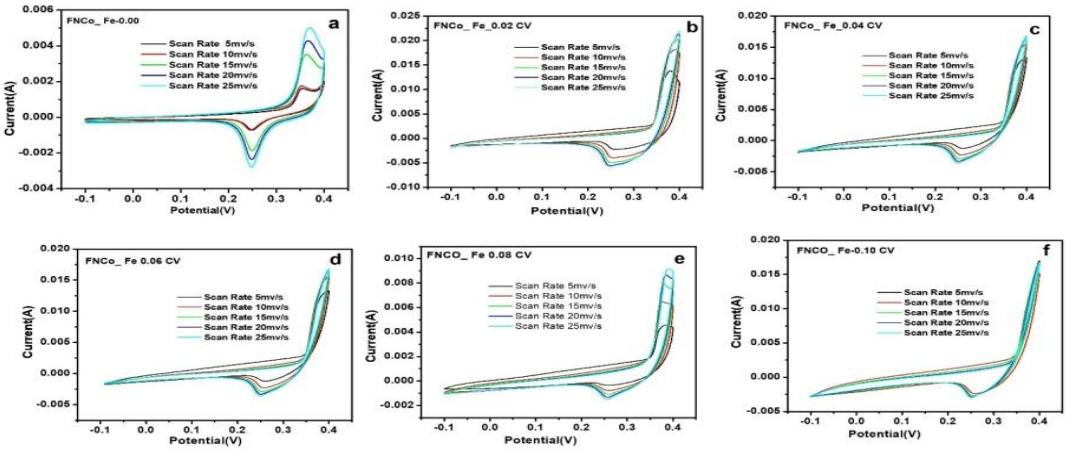

Figure 7(a-f): Cyclic voltammetry graphs plotted Current (I) vs Potential (V) of FNCO NPs for the scan rates of 5 mVs^{-1}, 10 mVs^{-1}, 15 mVs^{-1}, 20 mVs^{-1}, and 25 mV/s for various values of a).x = 0.0, b). 0.02, c). 0.04, d). 0.06, e). 0.08 and f). 0.10.

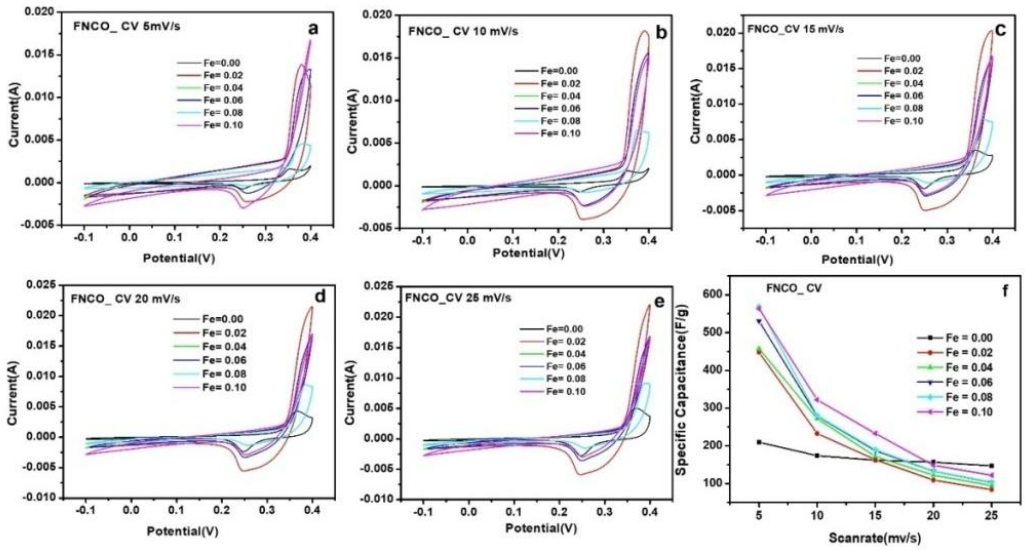

Figure 8 (a-f): Cyclic voltammetry graphs plotted Current (I) vs Potential (V) of FNCO NPs forthe scan rates of a). 5 mVs^{-1}, b). 10 mVs^{-1}, c). 15 mVs^{-1}, d). 20 mVs^{-1}, e). 25 mV/s, and f). Specific capacitance vs scan rate (mVs^{-1}) .

The FNCO NPs appear to have good redox peaks, demonstrating faradaic (battery-like) capacitive behaviour. As shown in Fig. 8(a-f), the CV analysis was conducted for the FNCO NPs for x = 0.0, 0.02, 0.04, 0.06, 0.08, and 0.10. It is noticed that the separation between the reduction and oxidation peaks becomes larger with the increase in current density as a function of scan rate. This separation in the redox peaks can be attributed to the polarization of the cell under the relatively high scan rate. Because of the kinetic irreversibility of the redox process, the oxidation and reduction maxima of their respective anodic and cathodic scans are not uniform [43]. The specific capacitance (C_s) derived from CV study is determined using formula [38]:

$$C_s = \frac{\int idv}{2m\Delta Vs} \qquad F\ g^{-1}\text{-------- (6)}$$

Where C_s- specific capacitance (F g^{-1}), m - mass of material coated on the electrode (mg), ΔV –Applied potential window and V_s - scan rate (mVs^{-1})

Table 3: Scan rate and Specific Capacitance values (Cs) at different FNCO NPs for x = 0.0, 0.02, 0.04, 0.06, 0.08 and 0.10.

Sl. No.	Fe doping, x	Specific Capacitance, C_s (F g^{-1})				
		5 mV s^{-1}	10 mV s^{-1}	15 mV s^{-1}	20 mV s^{-1}	25 mV s^{-1}
1	0.00	209.39	173.91	161.93	156.75	146.66
2	0.02	448.12	232.64	151.70	109.33	84.01
3	0.04	457.01	272.11	172.19	122.27	94.87
4	0.06	707.65	315.70	199.66	141.72	109.94
5	0.08	568.50	279.86	182.73	133.24	103.77
6	0.10	603.70	333.32	207.73	127.39	87.19

However, even at higher scan rates, the form of the redox peaks stays similar without distortion, showing the outstanding reversibility and rate capability of the working electrode materials. The contrast of FNCO NPs at various scan rates (5 - 25 mVs^{-1}) is also shown in Fig. 7(a-f). The area enclosed by FNCO NPs is greater than the area enclosed by pure NCO NPs, indicating that these electrode materials have the greatest charge storing capacity. The rise in Fe doping content causes agglomeration, which reduces the electrical activity of the as-prepared nanoparticles.

The obtained values of C_s are decreased from 707.65 F g^{-1} to 87.19 F g^{-1}. The maximum C_s was obtained at the scan rate 5 mVs^{-1} for x=0.06 and minimum was obtained for x = 0.10 at a scan rate 25 mVs^{-1}. The decrease in C_s has been attributed to the presence of inner active sites that cannot sustain the redox transitions completely at higher scan rates. This is probably due to the diffusion effect of protons within the electrode. The decreasing trend of the C_s suggests that parts of the surface of the electrode are inaccessible at high charging–discharging rates [44]. If the doping concentration decreases, there is insufficient redox active site to contribute into the electrochemical activity which leads to poor specific capacitance (C_s) [45].

In contrast, the impact of Fe doping produces multivalent cations to add to electrochemical processes and increases redox activity through a synergistic effect between the Fe ions and the NCO structure. Furthermore, the creation of mesoporous cubic shaped FNCO results in high C_s, good electrode stability, and excellent reversibility at higher scan rates due to better ionic transport via the porous structures and excellent electrical conductivity. At various scan rates, the C_s of the electrode materials was determined using supplementary information Eq. 6, and the results are presented in Table 3.

The Galvanostatic charge-discharge (GCD) profiles of FNCO at a current density of 1 Ag^{-1}in a potential window of 0 to 1.0 Vare shown in Fig. 9. The emergence of a non-linear

shape verifies the faradaic character of the materials which is consistent with the CV curve. Further, the cycling stability of the FNCO was analyzed at 1 Ag^{-1}.

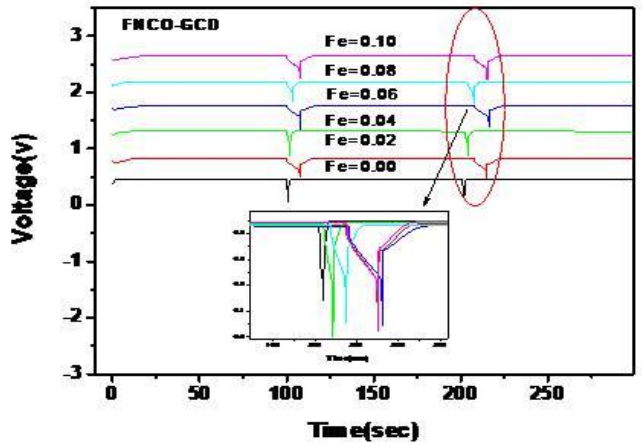

Figure 9: Galvanometric charge-discharge (GCD) plots with Potential on Y-axis and Time on X-axis of FNCO NPs with various values of x = 0.0, 0.02, 0.04, 0.06, 0.08 and 0.10.

The GCD cycle test results show that the impact of Fe doping increases the redox active sites when compared to pure NCO, resulting in improved cycling performance, stability, and longevity of the as-prepared electrode material. When compared to previous results of NCO nanoparticles with mesoporous carbon composites (C/NCO), the acquired C_s and capacitive retention of FNCO are significant value at the current density 1 A g^{-1} [46].The specific capacitance (C_s) was determined by GCD test using the following formula:

$$C_s = \frac{I\Delta t}{m\Delta v} F\ g^{-1} \quad \text{--------- (7)}$$

Where, C_s - specific capacitance of active materials, I = current applied,
Δt = discharge time duration, m = mass of active material loaded on Ni- foam and
ΔV - Applied potential window (V_2-V_1)

The Table 4 displays the computed Specific capacitance of FNCO NPs and calculated values of Energy and Power densities. The calculated C_s for x = 0.06 for FNCO demonstrated the better GCD characteristics, with a high C_s of 640.36 F g^{-1} at a current density of 1 Ag^{-1}. The table shows the precise C_s values for x = 0.0, 0.02, 0.04, 0.06, 0.08, and 0.10. The high C_s achieved for x = 0.06 doped with FNCO NPs may be due to the significantly extended intercalation of Ni^{2+} or Co^{2+} ions during redox potential, which allows the ions to reach the active sites in the working electrode, as well as the uniform spherical formation of NCO nanoparticles, which can facilitate the improved electrochemical properties of the obtained product.

Table 4: Calculated values of Specific capacitance, Energy density and Power density using GCD test of FNCO NPs for x = 0.0, 0.02, 0.04, 0.06, 0.08 and 0.10

Sl. No.	Fe Doping, x	$C_s = \frac{I\Delta t}{m\Delta v}$ (F g^{-1})	$E_d = \frac{1}{2} Cs((\Delta V)^2) * (\frac{1}{3.6})$ (Wh kg^{-1})	$P_d = \frac{E_d}{\Delta t} * 3600$ (W kg^{-1})
1	0.00	205.46	4.54	199.50
2	0.02	219.81	5.57	213.55
3	0.04	314.53	6.34	238.13
4	0.06	640.36	17.30	630.00
5	0.08	513.86	10.20	378.00
6	0.10	563.87	11.91	433.33

The Energy density was calculated with the help of this formula Energy density [47],

$E_d = \frac{1}{2} Cs((\Delta V)^2) * (\frac{1}{3.6})$ Wh kg^{-1}--------- (8)

and

Power density, $P_d = \frac{Ed}{\Delta t} * (3600)$ W kg^{-1} -------- (9)

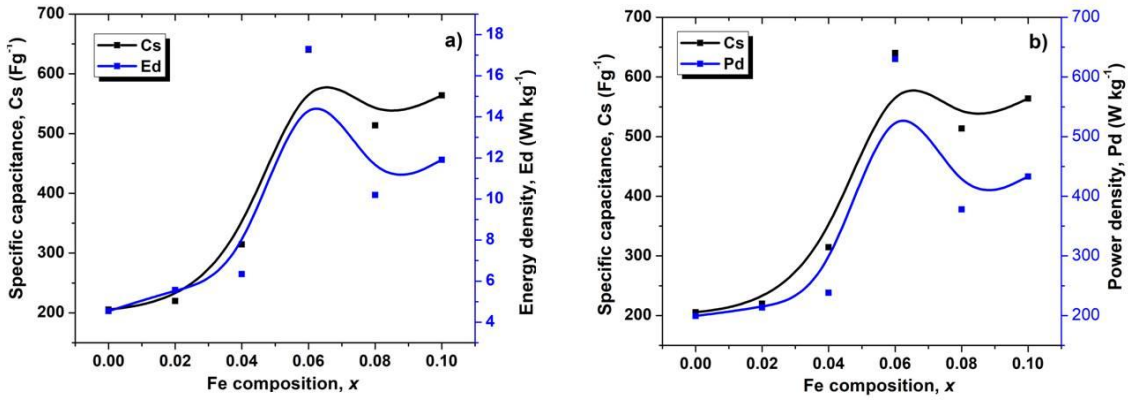

Figure 10 (a-b): Variation of a). Energy density (E_d) and b). Power density (P_d) vs Specific capacitance (C_s) of FNCO NPs at a current density of 1 A g^{-1}

The Fig. 10(a) shows the Specific capacitance (C_s)and Energy density (E_d) values versus Fe composition in FNCO samples at a current density of 1 A g^{-1}. Which shows that as Fe composition increases, the both C_s and E_d increases rapidly up to x = 0.06 and then becomes stable. This might be due to FNCO's high electrical conductivity at x = 0.06. The Fig. 10(b) shows the C_s and Power density (P_d) values versus Fe composition in FNCO samples at a current density of 1 A g^{-1}. Which shows that as Fe composition increases, the both C_s and P_d increases rapidly up to x = 0.06 and then becomes stable. It found that the highest values of E_d and P_d are 630 W kg^{-1} and 17.40 Wh kg^{-1}, respectively.

The electrical behaviour of any substance can be investigated by measuring its resistance. Impedance is a complex number that can be expressed as Z = Z′ + Z″, where Z′ represents resistance (real part of impedance) and Z″ represents reactance (imaginary part of impedance). Fig. 10 depicts the real (Z′) and imaginary (Z") impedance portions of FNCO NPs. It was noted that as frequency increased, the impedance of synthesized substance dropped.

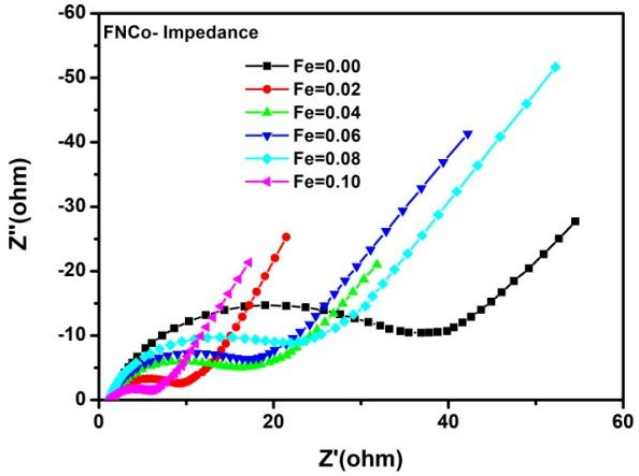

Figure 11: The Impedance graphs plotted Real impedance (Z′) and imaginary impedance (Z″) for FNCO NPs for x = 0.0, 0.02, 0.04, 0.06, 0.08 and 0.10.

The conductivity of all FNCO was verified by a reduction in impedance. At low frequencies, all materials acted like resistive mediums, and their resistance dropped significantly as frequency increased. As a result, all of the samples acted like resistive mediums in the low-frequency region before transitioning to conductive mediums as the frequency increased. Furthermore, the impedance of NCO dropped with each stage of Fe substitution. Complex impedance readings are useful for distinguishing grain resistance from grain boundary areas. The Cole-Cole plot is shown in Fig.11 which is drawn between Z′ along the X-axis and Z″ along the Y-axis. In general, information about three distinct electro- active areas can be derived from these plots. These various areas include conducting grains, insulating grain boundaries, and the contact regionbetween samples and electrodes. The semicircle represents charge-transfer impedance at the electrode-electrolyte contact [48]. Because there is a clear relationship between the width of a semicircle and the resistance of the object, at x = 0.0, the compound exhibits extremely insulating behaviour. Nonetheless, as the Fe content in the samples rose, the diameter of the semicircles decreased. As a result, it is possible to infer that the decline in diameter represented a decrease in resistivity and an increase in conductivity of the specimens.

4. Conclusions

It was discovered that the samples under study formed a cubic-spinel lattice and that for x = 0.06 exhibited superior GCD characteristics with a high specific capacitance of 640.06 F g^{-1} at a current density of 1 A g^{-1}. The energy and power densities are 17.30 Wh kg^{-1}, 630 W kg^{-1} respectively. The impedance decreased with increasing frequency for all FNCO compositions. It was also discovered that, the sample for x = 0.10 shown highly conductive in nature. The energy and power densities increase with increasing the specific capacitance.

References

[1] Pravalika Butreddy, Swaroop Chakraborty, Pushpanjali Soppina, Rakesh Behera, Virupakshi Soppina, Superb K Misra, Novel dual labelled nanoprobes for nanosafety studies: Quantification and imaging experiment of CuO nanoparticles in C. elegans. Chemosphere, (2022), 286, 131698-131706.

[2] Pravalika Butreddy, Selina Laws, Premitha Pansalawatte, Eric Laws and Hemali Rathnayake, Supramolecular Chemistry of Folic Acid - Experimental and Computational Investigation, Biophy. Rev. and Letters, (2021), 16(3), 95-109.

[3] X.Y. Liu, S.J. Shi, Q.Q. Xiong, L. Li, Y.J. Zhang, H. Tang, C.D. Gu, X.L. Wang, J.P. Tu, Hierarchical $NiCo_2O_4$@$NiCo_2O_4$ core/shell nanoflake arrays as high-performance supercapacitor materials,ACS Appl. Mater. Interfaces, (2013), 5(17), 8790–8795.

[4] J.P. Wang, S.L. Wang, Z.C. Huang, Y.M. Yu, J. Mater, Hierarchical $NiFe_2O_4$/Fe_2O_3 nanotubes derived from metal organic frameworks for superior lithium-ion battery anodes, Chem. A, (2014), 2, 8048-8053.

[5] John R. Miller, Patrice Simon, Electrochemical Capacitors for Energy Management, Science, (2008), 321, 651-652.

[6] Y.Q. Zhang, X.H. Xia, J.P. Tu, Y.J. Mai, S.J. Shi, X.L. Wang, C.D. Gu, Self-assembled synthesis of hierarchically porous NiO film and its application for electrochemical capacitors, J. Power Sources, (2012), 199.

[7] J.B. Han, Y.B. Dou, J.W. Zhao, M. Wei, D.G. Evans, X. Duan, Flexible CoAl LDH@PEDOT core/shell nanoplatelet array for high-performance energy storage. Small, (2013), 9.

[8] X.H. Lu, T. Zhai, X.H. Zhang, Y.Q. Shen, L.Y. Yuan, B. Hu, L. Gong, J. Chen, Y.H. Gao, J. Zhou, Y.X. Tong, Z.L. Wang, WO_{3-x}@Au@MnO_2 Core–Shell Nanowires on Carbon Fabric for High-Performance Flexible Supercapacitors, Adv. Mater, (2012), 24.

[9] Xin Chen , Hui Li, Jianzhou Xu, F. Jaber, F. Musharavati, Erfan Zalezhad, S. Bae, K.S.Hui, K.N. Hui and Junxing Liu, Synthesis and Characterization of a $NiCo_2O_4$@$NiCo_2O_4$ Hierarchical Mesoporous Nanoflake Electrode for Supercapacitor Applications, Nanomaterials,(2020), 10, 1292

[10] Y. Yang, D. Zeng, S. Yang, L. Gu, B. Liu, S. Hao,Nickel cobaltite nanosheets coated on metal-organic framework-derived mesoporous carbon nanofibers for high-performance pseudocapacitors, J. Colloid Interf. Sci., (2019), 534, 312–321.
[11] T.Y. Wei, C.H. Chen, H.C. Chien, S.Y. Lu, C.C. Hu,A cost-effective supercapacitor material of ultrahigh specific capacitances: Spinel nickel cobaltite aerogels from an epoxide-driven sol-gel process, Adv. Mater, (2010), 22.
[12] H. Jiang, J. Ma, C.Z. Li, Hierarchical porous $NiCo_2O_4$ nanowires for high-rate supercapacitors, Chem. Commun. (2012), 48.
[13] L. L. Li, Y. L. Cheah, Y. W. Ko, P. F. Teh, G. Wee, C. L. Wong, S. J. Peng and M. Srinivasan,The facile synthesis of hierarchical porous flower-like $NiCo_2O_4$ with superior lithium storage properties, J. Mater. Chem. A, (2013), 1(36), 10935-10941.
[14] L.F. Hu, L.M. Wu, M.Y. Liao, X.S. Fang,High-performance $NiCo_2O_4$ nanofilm photodetectors fabricated by aninterfacial self-assembly strategy, Adv. Mater, (2011), 23, 1988–1992.
[15] Y.G. Li, P. Hasin, Y.Y. Wu, $NixCo_{3-x}O_4$ Nanowire arrays for electrocatalytic oxygenevolution, Adv. Mater, (2010), 22, 1926–1929.
[16] Q.A. Pankhurst, J. Connolly, S.K. Jones, J. Dobson, Applications of magnetic nanoparticles in biomedicine, J. Phys. D-Appl. Phys. Journal of Physics D, Applied physics, (2003), 36,13.
[17] Y.Q. Wu, X.Y. Chen, P.T. Ji, Q.Q. Zhou, Sol–gel approach for controllable synthesis and electrochemical properties of $NiCo_2O_4$ crystals as electrode materials for application in supercapacitors, Electrochim. Acta, (2011), 56, 7517-7522.
[18] L. Qian, L. Gu, L. Yang, H.Y. Yuan, D. Xiao, Direct growth of $NiCo_2O_4$ nanostructures on conductive substrates with enhanced electrocatalytic activity and stability for methanol oxidation, Nanoscale, (2013), 5, 7388–7396.
[19] Y. Lei, J. Li, Y.Y. Wang, L. Gu, Y.F. Chang, H.Y. Yuan, D. Xiao, Synthesis of 3D-Nanonet Hollow Structured Co_3O_4 for High Capacity Supercapacitor, ACS Appl. Mater. Interfaces, (2014), 6, 9, 6739–6747.
[20] N. Padmanathan, S. Selladurai, Controlled growth of spinel $NiCo_2O_4$ nanostructures on carbon cloth as a superior electrode for supercapacitors, RSC Adv,(2014), 4, 8341-8349.
[21] G.Q. Zhang, H.B. Wu, H.E. Hoster, M.B. Chan-Park, X.W. Lou,Single-crystalline $NiCo_2O_4$ nanoneedle arrays grown on conductive substrates as binder-free electrodes for high-performance supercapacitors, Energy Environ. Sci. (2012), 5.
[22] S. Verma, H.M. Joshi, T. Jagadale, A. Chawla, R. Chandra, S. Ogale, Nearly Monodispersed Multifunctional $NiCo_2O_4$ Spinel Nanoparticles: Magnetism, Infrared Transparency, and Radiofrequency Absorption, J. Phys. Chem.C (2008), 112.
[23] W.W. Zhou, D.Z. Kong, X.T. Jia, C.Y. Ding, C.W. Cheng, G.W. Wen,$NiCo_2O_4$nanosheet supported hierarchical core–shell arrays for high-performance supercapacitors, J. Mater.Chem.A, (2014), 2.
[24] X.X. Yu, J.G. Yu, B. Cheng, M. Jaroniec, Synthesis of Hierarchical Flower-like AlOOH and TiO_2/AlOOH Superstructures and their Enhanced Photocatalytic Properties, J. Phys. Chem. C, (2009), 113.
[25] T. Zhou, S. Cao, R. Zhang, J. Tu, T. Fei, T. Zhang,Effect of cation substitution on the as-sensing performances of ternary spinel $MiCo_2O_4$ (M= Mn, and Ni) multishelled hollow twin spheres, ACS Appl. Mater. Inter.,(2019), 11(31), 28023–28032.
[26] M. Yang, Y. Li, Y. Yu, X. Liu, Z. Shi, Y. Xing,Self-assembly of three-dimensional zinc-doped $NiCo_2O_4$ as efficient electrocatalysts for oxygen evolution reaction, Chem. Euro J. 24(49), (2018), 13002–13008.
[27] W. Shang, W. Yu, P. Tan, B. Chen, H. Xu, M. Ni,A highperformance Fe battery based on self-assembled nanostructured $NiCo_2O_4$electrode, J. Power Sources, (2019),421, 6–13.
[28] Wang H, Hu L, Wang C, Sun Q, Li H, Zhai T,High-loading individually dispersed $NiCo_2O_4$ anchoring on checkerboard-like C/CNT nanosheets as a binder-free high rate electrode for lithium storage, J Mater Chem A, (2019),7,3632–41.
[29] Wu X, Li Y, Zhao S, Zeng F, Peng X, Xiang Y, et al, Fabrication of F-doped, C-coated $NiCo_2O_4$ nanocomposites and its electrochemical performances for lithium-ion batteries, Solid-State Ionics, (2019), 334, 48–55.
[30] Yuan, C., Wu, H.B., Xie, Y., Lou, X.W. Anew, Mixed transition-metal oxides: design, synthesis, and energy-relatedapplications, Chem. Int. Ed, (2014), 53, 1488–1504.
[31] Wang, J., Zhang, Q., Li, X., Xu, D., Wang, Z., Guo, H., Zhang, K.Three-dimensional hierarchical Co_3O_4/CuO nanowire heterostructure arrays on nickel foam for high-performance lithium-ion batteries Nano Energy, (2014), 6, 19–26.
[32] Wei, T.Y., Chen, C.H., Chien, H.C., Lu, S.Y., Hu, C.C.A cost-effective supercapacitormaterial of ultra-highspecific capacitances: spinel nickel cobaltite aerogels from an epoxide-driven sol-gel process, Adv. Mater, (2010), 22, 347–351.
[33] Hu, L., Wu, L., Liao, M., Hu, X., Fang, X, Electrical Transport Properties of Large, Individual$NiCo_2O_4$Nanoplates, Adv.Funct. Mater, (2012), 22, 998–1004.
[34] J. Singh, C. Singh, D. Kaur, H. Zaki, I.A. Abdel-Latif, S.B. Narang, R.B. Jotania, S.R. Mishra, R. Joshi, P. Dhruv, M. Ghimire, S.E. Shirsath, S.S. Meena, Elucidation of phase evolution, microstructural, Mossbauer and magnetic properties of Co^{2+}-Al^{3+} doped M-type BaSr hexaferrites synthesized by a ceramic method, J. Alloys. Compd. (2017), 695, 1112–1121.
[35] T.L. Ajeesha, A. Anantharaman, J.N. Baby, M. George, Structural, magnetic, electrical and photo-Fenton properties of copper substituted strontium M-hexagonal ferrite nanomaterials via chemical Co precipitation approach, J. Nanosci. Nanotechnol, (2020), 20, 1589–1604.
[36] Y.C. Wong, J. Wang, G. Bee Teh, Structural and magnetic studies of $SrFe_{12}O_{19}$ by sol-gel method, Proc. Eng, (2014), 76, 45–52.
[37] S. Katlakunta, S.S. Meena, S. Srinath, M. Bououdina, R. Sandhya, K. Praveena, Improved magnetic

properties of Cr^{3+}doped $SrFe_{12}O_{19}$ synthesized via microwave hydrothermalroute, Mater. Res. Bull, (2015), 63, 58–66.

[38] S. Vijayakumar, S. Nagamuthu, G. Muralidharan, Supercapacitor studies on NiO nanoflakes synthesized through a microwave route, ACS Appl. Mater. Interfaces, (2013), 5, 2188–2196.

[39] Liu, L., Wang, J., Hou, Y., Chen, J., Liu, H.K., Wang, J., Wu, Y, Self-Assembled 3D Foam-Like $NiCo_2O_4$ as Efficient Catalyst for Lithium Oxygen Batteries, Small, (2016), 12, 602–611.

[40] Monte, M. Munuera, G., Costa, D., Conesa, J.C, Arias, A.M, Near-ambient XPS characterization of interfacialcopper species in ceria-supported copper catalysts, Phys. Chem. Chem. Phys, (2015), 17, 29995–30004.

[41] Waghmode, Ratnamala and Torane, Role of deposition time on synthesis of high-performance $NiCo_2O_4$ supercapacitors, A. Materials in Electronics,(2017), 28. 1-9.

[42] Ramesh J. Deokate, Chemically deposited $NiCo_2O_4$ thin films for electrochemical study, ES Materials and Manufacturing, (2021), 11, 16-19.

[43] Amri, A., Jiang, Z.T., Zhao, X,Xie, Z., Yin, C.Y., Ali, N., Mondinos, N., Rahman,M.M., Habibi, D,Tailoring the physicochemical and mechanical properties of optical copper–cobalt oxide thin films through annealing treatment, Surf. Coat. Technol, (2014), 239, 212–221.

[44] B. Chi, J. Li, Y. Han, Y. Chen,Effect of temperature on the preparation and electrocatalytic properties of a spinel $NiCo_2O_4$/Ni electrode, Int. J. Hydrogen Energy, (2004), 29, 605-610.

[45] R. Roshani, A. Tadjarodi,Synthesis of $FeFe_2O_4$ nanoparticles with high specific surfacearea for high-performance supercapacitor, J. Mater. Sci. Mater. Electron. (2020), 31(4), 23025–23036.

[46] S. S. Pradeepa, P. Rajkumar, K. Diwakar, K. Sutharthani, R. Subadevi, and M. Sivakumar, ChemistrySelect, (2021), 6, 6851- 6862.

[47] Ping Xia, Qiyuan Wang, Yintao Wang, Wei Quan, Deli Jiang, Min Chen, Journal of Alloys and Compounds, (2019), 771, 784-792.

[48] R.J. Gilliam, J.W. Graydon, Wang, X., Xiao, Y.,Su, D.; Zhou, L., Wu, S., Han, L., Fang, S., Cao, High-quality Porous Cobalt Monoxide Nanowires @ Ultrathin Manganese dioxide Sheets Core-Shell Nanowire Arrays on Ni Foam for High-Performance Supercapacitor,S. Electrochim. Acta,(2016), 194, 377−384.